Flow field evolution and entrainment in a free surface plunging jet

Syed Harris Hassan,[1] Tianqi Guo,[2] and Pavlos P. Vlachos[2,*]
[1]*School of Engineering, RMIT University, 124 La Trobe Street, Melbourne VIC 3000, Australia*
[2]*School of Mechanical Engineering, Purdue University, 585 Purdue Mall, West Lafayette, Indiana 47907, USA*

(Received 11 March 2019; published 9 October 2019)

We investigate ambient fluid entrainment and near-field flow characteristics of a free surface plunging jet for five Reynolds numbers ranging from 3000 to 10 000 using time-resolved stereo particle image velocimetry. We present time-averaged velocities, rms velocity fluctuations, mean entrainment, and instantaneous flow structures in the near-field for plunging jets, and compare the results with previous studies on free jets. It is found that additional instabilities accumulated from the free surface facilitate vortex development, leading to early initiation of bulk fluid entrainment, and finally result in expedited closure of the shear layer, which is absent for submerged free jets. These primary vortices are formed right below the free surface and disintegrate into secondary structures at axial locations that are upstream compared to those of free jets. As a result, plunging jets have a smaller potential core length, exhibit earlier decay of the mean centerline velocity and entrain more liquid from the ambient. Moreover, the peak rms velocity fluctuations occur at locations significantly more upstream than in free jets. For the plunging jet case at Re = 3000, faster jet decay, higher levels of turbulent intensity in the near field, and augmented mass entrainment result from strong primary vortices that give the turbulent-nonturbulent interface its convoluted shape, which facilitates both bulk entrapment of ambient fluid and small-scale nibbling because of larger surface area. At higher Reynolds numbers, primary vortices are smaller in size, weak in swirling strength, and disintegrate prematurely, resulting in suppressed mixing and reduced entrainment efficiency.

DOI: 10.1103/PhysRevFluids.4.104603

I. INTRODUCTION

A plunging jet consists of a free jet that exits from a nozzle and plunges into a quiescent pool of fluid from a certain height. This phenomenon is abundant in nature and is also encountered in various industrial processes. Hydraulic jumps and waterfalls are examples of this phenomenon occurring naturally whereby they contribute to river oxygenation, which is crucial for the underwater ecosystem. Industrial processes such as wastewater discharge, sump discharge, aeration of chemical reactions for gas absorption, or mixing and pouring of molted metals and plastics involve plunging jets [1]. Such easy-to-generate flows are valuable owing to their mixing efficiency by exchanging mass, momentum, and heat. Studying these flows is therefore important in order to understand and control natural phenomena and design engineering applications. Moreover, plunging jets are important from the scientific standpoint as they involve interaction of a free jet with a gas-liquid interface, which generates a complex multiphase, three-dimensional, and turbulent flow field that gives rise to numerous interesting questions [2].

*pvlachos@purdue.edu

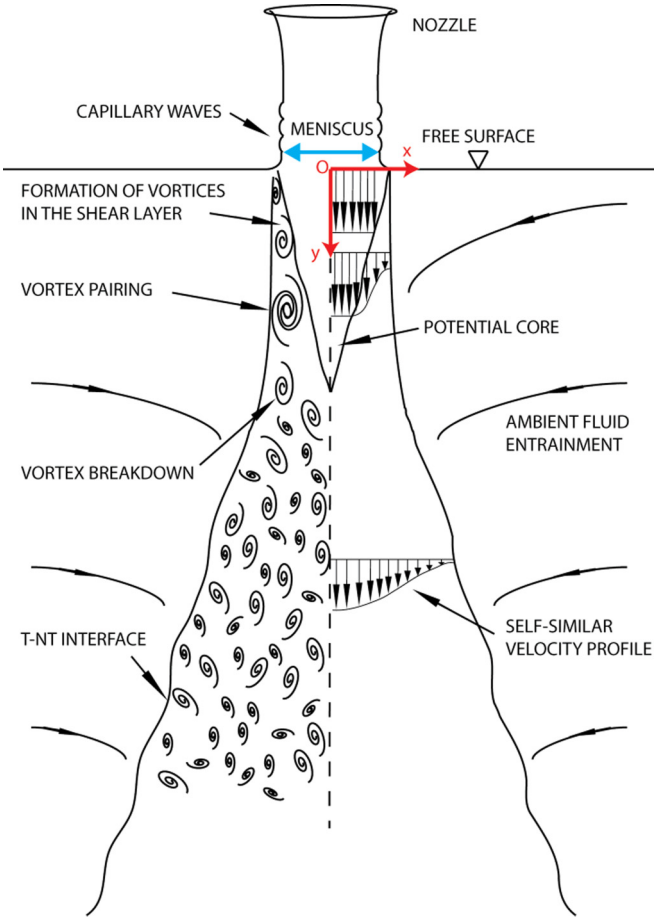

FIG. 1. Schematic diagram of a plunging jet.

Figure 1 illustrates a plunging jet as it exits the nozzle. The x and y coordinates correspond to the axial and radial directions, and the out-of-plane (azimuthal) direction is indicated by the z coordinate. As the jet travels downward, the liquid column undergoes acceleration due to gravity, resulting in an increase in the jet velocity and a decrease in its diameter [3]. Capillary waves form at the column base, followed by an increase in its diameter before impacting the free surface [4]. Beneath the free surface, the plunging jet evolves similar to a free jet whereby the axial velocity decreases with depth and the velocity profiles spread out due to diffused momentum and entrainment of ambient liquid. As the jet penetrates the free surface, the velocity difference between the potential core and ambient fluid results in the roll-up of the shear layer into primary vortical structures that resemble toroidal rings [5–9]. Formation of these vortices is due to growth of the Kelvin-Helmholtz instability [7–9]. As the primary vortices travel downward, they grow in size and entrain ambient fluid toward the jet core resulting in its erosion and eventual termination [7–11]. This growth is both linear and symmetrical both toward and away from the potential core. Apart from interacting with the potential core, primary vortices also interact with each other due to mutual induction and undergo pairing [5,7,9]. These pairing events happen single or multiple times depending on the Reynolds number [12,13]. Studies have also shown secondary streamwise vortices or braids are responsible for further entrainment of ambient fluid toward the jet [8,9,14,15]. With the end of the potential core, the centerline velocity decays, resulting in weakened shear. Consequently, primary

vortices become unstable and disintegrate into smaller secondary structures that move downstream leading to fully developed turbulent flow [6,8].

Ambient fluid entrainment plays a crucial role in the decay and spreading of both free and plunging jets. The term entrainment comprises all mechanisms through which irrotational ambient fluid is incorporated into the turbulent region [16]. One of the earliest studies to measure entrainment in free jets was by Ricou and Spalding in 1960 [17]. They designed a novel apparatus consisting of a porous-walled cylindrical chamber surrounding the jet. Since the chamber length was comparable to the jet length, they established a mean value for the entrainment coefficient (the derivative of normalized entrainment rate) and reported an average value of $C_E = 0.32$. All their experiments were performed for $\mathrm{Re} > 25\,000$, beyond which entrainment remained constant. Hill [18] modified the porous-walled apparatus by reducing the chamber height which enabled measurement of local entrainment rates by moving the chamber axially downstream from the nozzle. Experiments were performed for $\mathrm{Re} > 60\,000$, and results indicated that the local entrainment coefficient started with a value of $C_E = 0.1$ at $y/D = 2$ from the nozzle and increased to 0.32 at $y/D = 13$, which was in agreement with Ricou and Spalding [17]. Liepmann and Gharib [8] were the first to investigate this problem using particle image velocimetry (PIV) and discussed the role of streamwise vortex pairs (braids) in the near-field entrainment of round jets. They showed that these braids develop from wavelike instabilities in the shear layer and play a major role in an inward flow of ambient fluid around the jet via streamwise vorticity. Han and Mungal [19] quantified ambient fluid entrainment in a free jet subjected to coflow by direct PIV measurements. Although their entrainment coefficient agreed with Ricou and Spalding [17], it took 35 diameters to converge rather than 13 as reported by Hill [18]. El Hassan and Meslem [15] studied the effect of nozzle geometry on the near-field entrainment of a free jet at $\mathrm{Re} = 9500$ through stereo PIV. Lobed and chevron nozzles were found to produce streamwise vortices more efficiently than round nozzles, resulting in much higher entrainment rates. This was in agreement with Liepmann and Gharib [8] that streamwise structures enhance near-field entrainment for free jets.

While our understanding of the flow characteristics and ambient fluid entrainment for free jets is comprehensive, similar questions for plunging jets have not been addressed in detail. Most of the literature regarding plunging jets has focused on air entrainment mechanisms [20–22], bubble size distribution [23,24], bubble penetration depth [25,26], mean residence time of air entrained [27,28], and mixing characteristics [20,22]. Very few studies have been dedicated to the flow field development of the plunging jet itself [29,30], especially in the absence of air entrainment, and to the best of our knowledge, there has been very little study on ambient fluid entrainment for plunging jets. Considering these research gaps, this work investigates the flow field of a plunging jet using time-resolved stereo particle image velocimetry (SPIV) at nozzle Reynolds number between 3000 and 10 000. We quantify statistical flow properties such as mean centerline velocity decay, rms velocity fluctuations, and mean entrainment of plunging jets, and compare them to previous studies on free jets over a wide range of Reynolds numbers. In addition, the unsteady flow behavior involving vortex dynamics is also investigated and discussed.

II. EXPERIMENTAL APPARATUS AND PROCEDURES

A. Flow loop

Experiments are performed in a 0.3 m × 0.2 m × 0.3 m rectangular tank fabricated with clear acrylic sheets. A round and straight nozzle of inner diameter 7.8 mm is supported above the tank by an aluminum frame and carefully aligned perpendicular to the free surface by a spirit level. The height of the nozzle is adjusted at 2 nozzle diameters above the free surface. A gear pump (Model: C.P.78004-02) with pump head (Model: GB.P35.JSV.A) is used to generate a recirculating flow. To keep the water level constant, water was pumped out from the bottom of the tank through a pipe that was 6 times the diameter of the nozzle and rerouted to the jet nozzle. Experiments were conducted at room temperature (about 25 °C) at five nozzle Reynolds numbers ($\mathrm{Re_N} = 3000$, 4000, 6000, 8000,

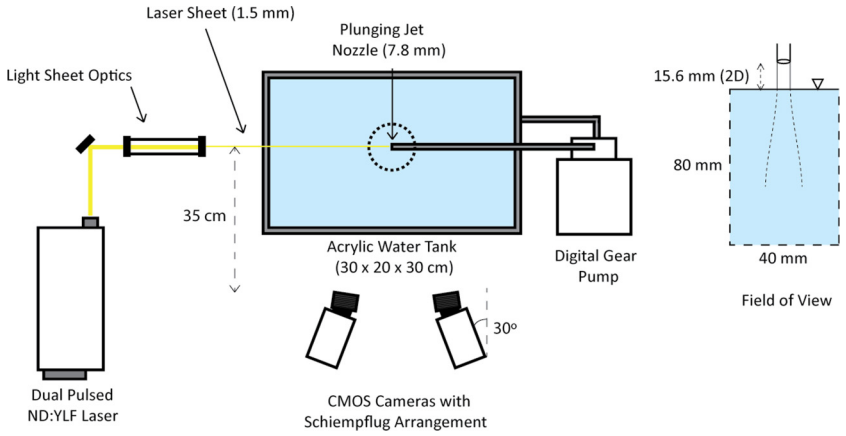

FIG. 2. Schematic diagram of the experimental setup.

and 10 000). Within this range the pump gives a stable fluid column, and there are no entrained air bubbles below the free surface. Figure 2 shows the schematic diagram of the setup.

B. Time-resolved stereoscopic measurements

Neutrally buoyant spherical polystyrene particles (Duke Scientific, density of 1.05 g/cm^3) 7 μm in diameter are homogeneously dispersed in the tank for flow seeding. Illumination is provided by a 527-nm, dual pulse Nd:YLF (neodymium:yttrium lithium fluoride) laser (Continuum Terra PIV 527-80-M). The laser beam is converted into a 1.5-mm-thick light sheet using two spherical and one cylindrical lens. The particle-scattered light is recorded by two high-speed CMOS (complementary metal-oxide-semiconductor) cameras (Phantom Miro M340, Vision Research, 1300 $\times$ 2560 pixels) mounted at an angle of 30° and at approximately 35 cm from the light sheet. Nikon objectives of 105 mm focal length and an aperture value of $f\#$ 8 are used with Schiempflug adapters [31]. The resulting field of view below the free surface is 40 mm $\times$ 80 mm. Both cameras and the laser are controlled by a synchronizer (TSI LaserPulse synchronizer 610036). For all tests, cameras are operated at $f = 980$ Hz, while laser pulse rate is varied accordingly to achieve particle displacement of around 7–8 pixels per frame near the free surface. The resulting double-frame temporal resolution of flow measurement is $\Delta t = 2/f = 2.04$ ms.

Stereoscopic camera calibration is performed using a dual-plane and dual-side calibration plate with 1.5-mm dots spaced at 1 cm (TSI). The calibration target is translated in the water tank by a micrometer traverse such that seven calibration planes are acquired by each camera (five planes inside the laser sheet and one on either side) with 0.381-mm out-of- plane increments. A polynomial mapping function (cubic in-plane and quadratic out-of-plane) is then employed with a self-calibration [32] refinement using 200 images to improve measurement accuracy. A total of 1200 image pairs are acquired for each test case, and then cross-correlated by LAVISION DAVIS 7.6 utilizing a multipass, iterative window deformation scheme with 32 $\times$ 32 window size and 50% overlap for the first three passes and a subsequent 16 $\times$ 16 window size and 50% overlap for the next three passes. After each pass, results are validated using velocity thresholding and universal outlier detection [33] to replace bad vectors. The final grid size is 4 $\times$ 4 pixels giving 665 $\times$ 358 vectors in the field of view.

C. Calculation of mean entrainment rate

Ambient fluid entrainment in jets can be directly measured through integration of mean velocity profiles obtained through PIV measurements [19,34].

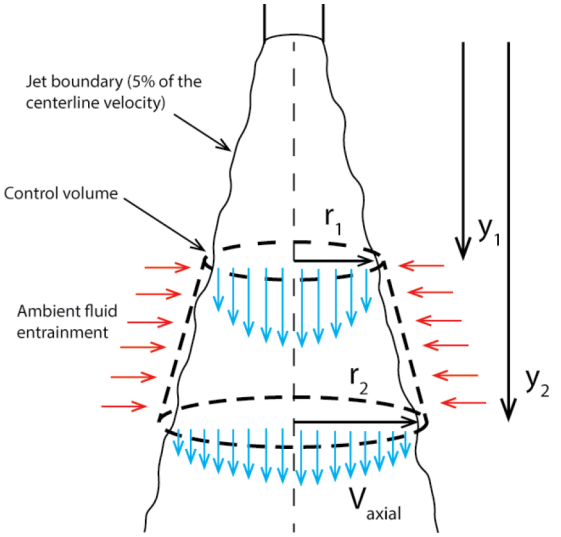

FIG. 3. Schematic diagram of the control volume used for entrainment evaluation from the axial velocity field.

Figure 3 shows a schematic diagram of the control volume defined by axial locations y_1 and y_2 and radial locations r_1 and r_2. Red arrows show the ambient fluid being entrained by the jet while blue arrows show the axial jet velocity. By mass conservation, the jet mass increase between y_1 and y_2 must be equal to the mass of the ambient fluid entrained radially through the control volume boundary. Mass flux entrained can then be calculated using the following equation,

$$\dot{m}_{\text{ent}} = \int_0^{r_2} \rho \overline{V}(y_2, r) 2\pi r dr - \int_0^{r_1} \rho \overline{V}(y_1, r) 2\pi r dr, \tag{1}$$

where ρ is the fluid density and $\overline{V}$ is the mean axial velocity obtained from 1200 snapshots of the velocity field. To use Eq. (1), it is essential to define a criterion to identify the jet boundary in terms of the axial velocity. In this work, this criterion is defined as the radial position where the axial velocity of the jet has reduced to 5% of the centerline velocity. Changing this criterion to 10% or 15% does not alter the comparison between the results of our plunging jets and the free jets from the literature. Values from Eq. (1) can further be used to calculate the local jet entrainment coefficient as defined by Ricou and Spalding [17],

$$C_E = \frac{d_0}{\dot{m}_0} \frac{d\dot{m}}{dx}, \tag{2}$$

where $\frac{d\dot{m}}{dx}$ represents the entrainment rate (the entrained mass flux per unit axial distance), and it is normalized by the jet diameter (d_0), and the initial mass flow rate (m_0). In this study, we calculate both the normalized mass flux and entrainment rate for all test cases.

D. Scaling of the plunging jet across the air-water interface

In studies on free jets, radial and axial distances are normalized by the nozzle diameter (D_N) which is constant for all Reynolds numbers. However, in plunging jets, the liquid column diameter downstream of the nozzle is a function of both the axial distance and Reynolds number. Figure 4 displays the relationship between the jet diameters (normalized by the nozzle diameter) before and after impact as the Reynolds number is increased from 3000 to 10 000.

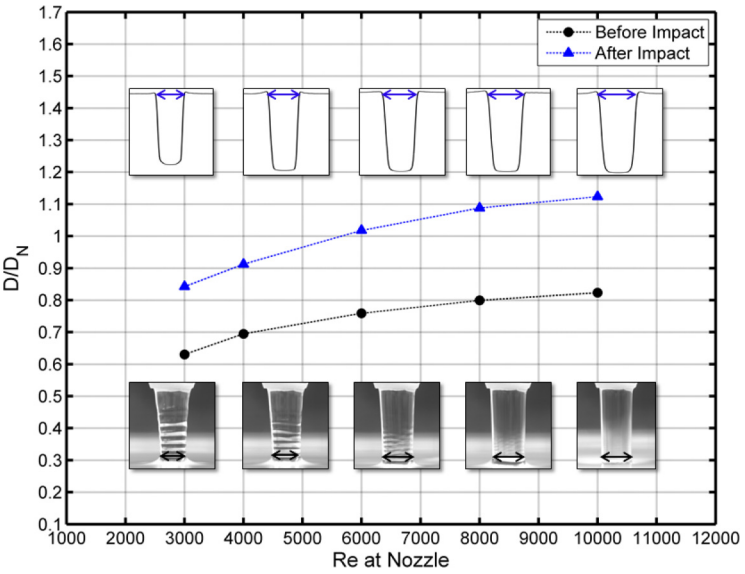

FIG. 4. Relationship between the plunging jet diameter and Reynolds number before and after impact.

The lower insets show the measurement location of the jet column diameter at the narrowest point above the meniscus before impact. Magnification calibration for this measurement is performed by placing a measurement scale in air beside the jet column. The postimpact plunging jet diameter is acquired by measuring the width of the axial velocity profiles right below the free surface (upper insets), and the magnification value is acquired from stereo PIV calibration. As the Reynolds number is increased, the postimpact jet diameter increases from 0.85 at $\mathrm{Re_N} = 3000$ to 1.12 at $\mathrm{Re_N} = 10\,000$. Moreover, increase in the plunging jet diameter across the free surface is approximately 33%–36% for all Reynolds numbers, which necessitates revision of length and velocity scaling. This revision is essential in order to compare our results with previous studies on free jets as it allows representing plunging jets with different nozzle velocities (V_N), nozzle diameters (D_N), and plunging heights (H) as free jets at the air-water interface with a certain diameter (D_{FS}) and velocity (V_{FS}). We introduce a new free surface Reynolds number ($\mathrm{Re_{FS}}$) in Eq. (3),

$$\mathrm{Re_{FS}} = \frac{\rho D_{\mathrm{FS}} V_{\mathrm{FS}}}{\mu}, \tag{3}$$

with values for each case shown in Table I. Nozzle jet velocities (V_N) from pump volumetric flow rates are used to estimate the increased velocities due to gravitational acceleration across the

TABLE I. Scaling of the plunging jet using parameters at the free surface.

Nozzle Reynolds number $\mathrm{Re_N}$	Nozzle jet velocity V_{N} (m/s)	Estimated velocity below free surface V_{est} (m/s)	Measured velocity below free surface V_{FS}(m/s)	Diameter below free surface D_{FS} (m)	Free surface Reynolds number $\mathrm{Re_{FS}}$
3000	0.34	0.65	0.70	0.0063	5004
4000	0.45	0.72	0.78	0.0069	6086
6000	0.68	0.88	0.98	0.0079	8774
8000	0.91	1.07	1.17	0.0084	10628
10000	1.14	1.27	1.37	0.0087	13292

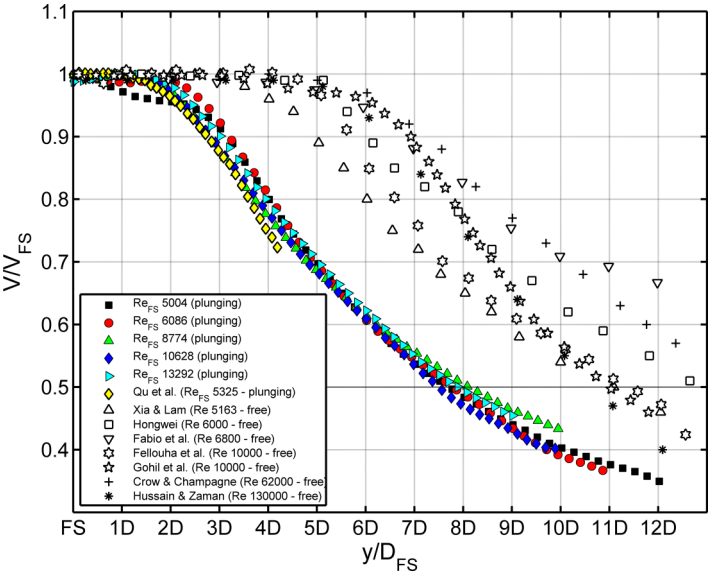

FIG. 5. Mean centerline velocity decay of the plunging jet cases normalized by the jet velocity at the free surface (V_{FS}). Representative results in the literature regarding free jets. (Note that to normalize the results from Qu *et al.* by D_{FS}, it is estimated from their setup that $D_{nozzle}/D_{FS} \approx 1.1$)

plunging heights by $V_{est} = \sqrt{V_N^2 + 2gH}$, which is within 10% difference when compared with the PIV-measured V_{FS}.

The physical quantities presented in this paper are therefore reported in nondimensional units divided by the jet diameter D_{FS} and jet velocity V_{FS} at the free surface.

III. RESULTS

A. Centerline velocity decay

Decay of mean centerline velocities of the plunging jet is illustrated in Fig. 5 (color symbols). Axial distance below the free surface and streamwise velocities are normalized by jet diameter (D_{FS}) and maximum streamwise velocity (V_{FS}) at the free surface. Representative results from the literature regarding decay of free jets are also shown (open symbols).

The axial distance where the mean streamwise velocity starts to decay is usually referred to as the length of the potential core, which is a conical region between the nozzle (or free surface in case of a plunging jet) and the closure point of shear layers [6–8,10]. For free jets in the literature, centerline velocity starts to decay in the range $y/D = 5$–7 [7,10,13,35–38], which is in sharp contrast to the plunging jets herein, where the centerline velocity in the potential core remains above $V/V_{FS} = 0.98$ until approximately $y/D_{FS} = 2$–2.5 for all cases except for $Re_{FS} = 5004$. For the latter case, an initial descent at $y/D_{FS} = 1$ is followed by a plateau where V/V_{FS} stays at 0.96 before the final decay starts at $y/D_{FS} = 2.5$. This behavior contradicts literature results at higher Reynolds numbers, where the centerline velocity stays constant until the decay region starts [7,13,35,39]. However, a recent study by Todde *et al.* [10] on free jets at Re = 1620–4050 reports a similar plateau in the initial region with periodic velocity modulation by mutual induction and pairing of strong ring vortices in this region. In later sections, we discuss similar primary vortices at $Re_{FS} = 5004$, a phenomenon significantly weaker for higher Re cases.

Beyond the potential core, velocity profiles of plunging jets decay significantly faster than free jets for all Reynolds numbers, which is indicated by the position where $V/V_{FS} = 0.5$. For plunging jets, this location is approximately 7.5–8D_{FS} below free surface, while for free jets this location

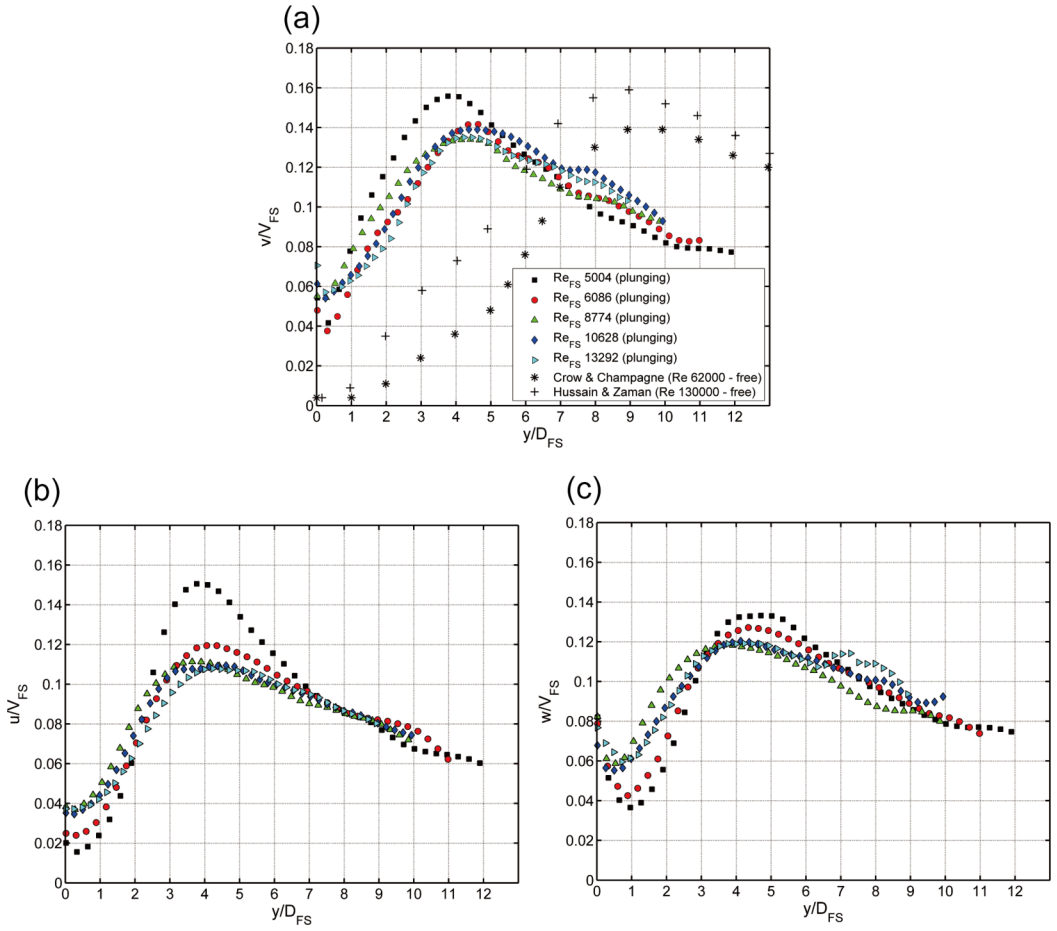

FIG. 6. rms of centerline velocity fluctuations for (a) axial, (b) radial, and (c) azimuthal directions compared with literature results on free jets.

lies between 11–13D. A similar premature decay of the centerline velocity was also reported by Qu *et al.* [30] (yellow symbols in Fig. 5) at Re = 5325 and a plunging height of $y/D = 2$ (same as our study). Early cessation of the potential core and rapid decay of the centerline velocity indicates faster development of plunging jets and therefore makes them less efficient than free jets in conserving momentum.

B. rms of centerline velocity fluctuations

Figure 6 shows the rms of jet centerline velocity fluctuations normalized by V_{FS} for the axial, radial, and azimuthal (out-of-plane) directions, respectively (color symbols), while representative results from the literature regarding axial rms fluctuations of free jets are shown in Fig. 6(a) (black symbols). Peak centerline rms velocity fluctuations have been associated with a rise in turbulent activity due to closure of the shear layers and the start of turbulent mixing throughout the jet [6,7,13,39]. Similar to the trend of mean centerline velocity decay, peak rms values in plunging jets appear significantly upstream ($y/D_{FS} = 4$–5) of the values reported for free jets in the literature ($y/D \sim 9$). This again demonstrates faster decay of plunging jets compared to free jets. The discrepancy in the initial values of rms velocity fluctuations near $y/D_{FS} = 0$ between free and plunging jets may be due to the plunging effect. For the plunging jet cases, significantly higher levels of axial and radial velocity fluctuations are observed for the $Re_{FS} = 5004$ case. Axial velocity

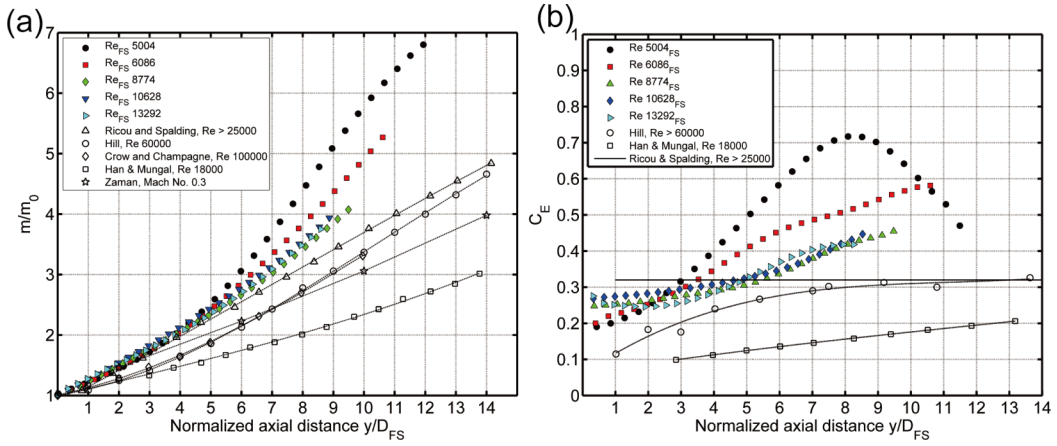

FIG. 7. (a) Mean entrainment rate (m/m_0) and (b) entrainment coefficient (C_E) of plunging jets compared with literature results on free jets.

fluctuations (v/V_{FS}) increase rapidly from 0.04 near the free surface and reach a peak of 0.16 at $y/D_{FS} = 4$, thereafter decreasing gradually to 0.08 at $y/D_{FS} = 12$ [Fig. 6(a)]. A similar pattern holds for the $Re_{FS} = 6086$, 8774, 10 628, and 13 292 cases, although their peak values are lower ($v/V_{FS} = 0.14$) and occur near $y/D_{FS} = 4.5$. Further downstream, the amplitudes decay in a linear fashion suggesting fully developed turbulent flow.

Centerline radial velocity fluctuations [u/V_{FS}, Fig. 6(b)] show a similar trend as axial fluctuations, with slightly lower magnitudes. At $Re_{FS} = 5004$, u/V_{FS} rises rapidly from 0.02 near the free surface to 0.15 at $y/D_{FS} = 4$, followed by a swift decrease to 0.10 at $y/D_{FS} = 7$ and finally a gradual decay to 0.06 at $y/D_{FS} = 12$. At $Re_{FS} = 6086$, u/V_{FS} attains a peak of 0.12 while in the latter three cases ($Re_{FS} = 8774$–13 292), peak values are slightly lower at 0.11, followed by a linear decay to 0.075 at $y/D_{FS} = 10$. Azimuthal velocity fluctuations [w/V_{FS}, Fig. 6(c)] have the same range as both axial and radial cases; however, the deviation of the $Re_{FS} = 5004$ case is not as pronounced with peak activity occurring at 0.135.

The deviation of the $Re_{FS} = 5004$ case in both axial (by 15%) and radial (by 35%) rms velocity fluctuations is in sharp contrast to previous investigations of free jets at high Reynolds numbers (Fig. 8 in Crow and Champagne [7]; Re: 62 000–124 000 and 2 in Hussain and Zaman [13]; Re: 32 000–113 000), where an order of magnitude change in the Reynolds number has little effect on the peak values. The behavior at $Re_{FS} = 8774$, 10 682, and 13 292 appears to be more consistent with the previous studies as velocity fluctuations become independent of the Reynolds number and collapse on top of each other. In a recent study, however, Reynolds number dependence of rms velocity fluctuation also exists for Re ~ 1000–6000 [10]. As will be discussed later, location of high rms velocity fluctuations at $Re_{FS} = 5004$ is consistent with the region where strong primary vortices disintegrate into small secondary structures, causing increase in the turbulent intensity and mixing.

C. Entrainment of ambient fluid

Figure 7(a) illustrates the mass entrainment ratio (m/m_0) obtained by averaging 1200 snapshots of axial velocity profiles integrated according to Eq. (1). Entrainment for all plunging jet cases stays close to the results of Ricou and Spalding [17] for the first 5 diameters, after which values start to diverge with the $Re_{FS} = 5004$ case rising steeply to $m/m_0 = 5$ at $y/D_{FS} = 9$, indicating that it has entrained 5 times its initial mass at a depth of 9 diameters. At the same depth, $Re_{FS} = 6080$ has entrained approximately 4.5 times its initial mass. Mass ratio profiles for the $Re_{FS} = 8774$, 10 628, and 13 232 cases collapse onto each other with $m/m_0 = 4$ at $y/D_{FS} = 9$.

In Fig. 7(b) the entrainment coefficient defined by Eq. (2) is plotted for comparison with literature results on free jets. The entrainment coefficient (C_E) quantifies the local rate at which mass is being entrained when compared to its initial mass flow rate (m_0). The entrainment coefficients obtained by Ricou and Spalding [17], Hill [18], and Han and Mungal [19] involving free jets all achieve a constant value of 0.32 in the far field, indicating a steady state has been reached. For plunging jet at $\mathrm{Re_{FS}} = 5004$, C_E starts with 0.2 near the free surface and undergoes a sharp increase at $y/D_{\mathrm{FS}} = 3$, reaching 0.72 at $y/D_{\mathrm{FS}} = 8$, followed by a descent to approximately 0.5 at $y/D_{\mathrm{FS}} = 12$. The C_E values for $\mathrm{Re_{FS}} = 6068$ show a gradual growth from 0.2 near the free surface to 0.45 at $y/D_{\mathrm{FS}} = 6$, thereafter growing linearly to approximately 0.6 at $y/D_{\mathrm{FS}} = 11$. Similar to the mass entrainment ratio profiles, C_E values of the $\mathrm{Re_{FS}} = 8774$, 10 628, and 13 292 cases collapse onto each other, starting with a higher value of approximately 0.27 near the free surface and reaching 0.45 at $y/D_{\mathrm{FS}} = 9$. Collapse of (m/m_0) and C_E profiles demonstrates that with increasing Reynolds number, mean entrainment reduces and eventually becomes invariant at $\mathrm{Re_{FS}} \sim 9000$. This is consistent with the results of Ricou and Spalding [17] who reported that the ratio m/m_0 became constant for free jets beyond Re = 25 000 (Fig. 3 of the cited paper). However, for plunging jets, Reynolds number independence occurs much earlier at $\mathrm{Re_{FS}} \sim 9000$. Due to a limited field of view in the axial direction, entrainment coefficient C_E values for all cases do not approach an asymptotic value; however, it has been established in numerous studies that the entrainment coefficients in all jets, irrespective of their initial conditions, do approach an asymptotic value (0.32 for free jet) when the flow achieves fully developed turbulence [8,16,18,19,40]. Overall, plunging jets at low Reynolds numbers are much more efficient in entraining ambient fluid in the near field, and an increase in the Reynolds number causes a decrease in the mean entrainment coefficient.

D. Unsteady flow behavior

The instantaneous flow organization of plunging jets is shown in Fig. 8 for the $\mathrm{Re_{FS}} = 5004$, 8774, and 13 292 cases in each row. The temporal sequence (separated by $3\Delta t = 6.12$ ms) consists of velocity vectors normalized by the jet axial velocity at the free surface (V_{FS}), with color contours representing the normalized swirling strength (λ_{ci}) calculated according to Zhou *et al.* [41]. The close-up views of the shear layer from the windows in Figs. 8(b), 8(e), and 8(h) are shown in Fig. 9.

Figures 8(a)–8(c) show three snapshots at $\mathrm{Re_{FS}} = 5004$. Strong primary vortices convect along the shear layer, growing in size as they entrain ambient fluid before becoming unstable and disintegrating into smaller secondary structures. Primary vortices induce a strong inward flow at their trailing edges along which ambient fluid is forced toward the jet core [red arrows in Fig. 9(a)]. This inward flow is called an entrainment zone or wedge and is inclined at an angle of approximately 45° from the jet axis [6]. In the range $y/D_{\mathrm{FS}} = 0.5$–1.2, two adjacent vortices undergo pairing [arrows A, Figs. 8(a)–8(c)], which occurs earlier than free jets in previous studies over a similar Reynolds number range. Liepmann and Gharib [8] reported that the first pairing event for a water jet at Re = 5500 usually takes place before 2.5 jet diameters while a recent study by Violato and Scarano shows occurrence between 2.7 and 3.5 diameters [9]. Pairing of the adjacent vortices in the shear layer occurs as a result of mutual induction whereby the downstream vortex induces an inward and axial flow at its trailing edge, causing an increase in the convective velocity of the upstream vortex. On the other hand, an opposite but less pronounced flow is induced by the upstream vortex at its leading edge as it pushes the flow outward, causing a decrease in the convective velocity of the upstream vortex [9]. Eventually, as a consequence of the difference in the convective velocity of the two adjacent vortices, a pairing event occurs. Subsequently, the resulting single vortex increases in size and convects downstream until $y/D_{\mathrm{FS}} = 2.5$–3.0 before disintegrating into smaller secondary structures [arrows B, Figs. 8(a)–8(c)].

For the latter cases at $\mathrm{Re_{FS}} = 8774$ and 13 292, primary vortices are smaller in size and have low swirling strength compared to the previous case. Overall arrangement of the shear layer is disorganized with numerous smaller vortical structures accompanying the primary vortices as they convect downstream. Often a "vortex train" appears below the free surface where primary vortices interact and then quickly disintegrate into smaller secondary structures. Smaller primary vortices

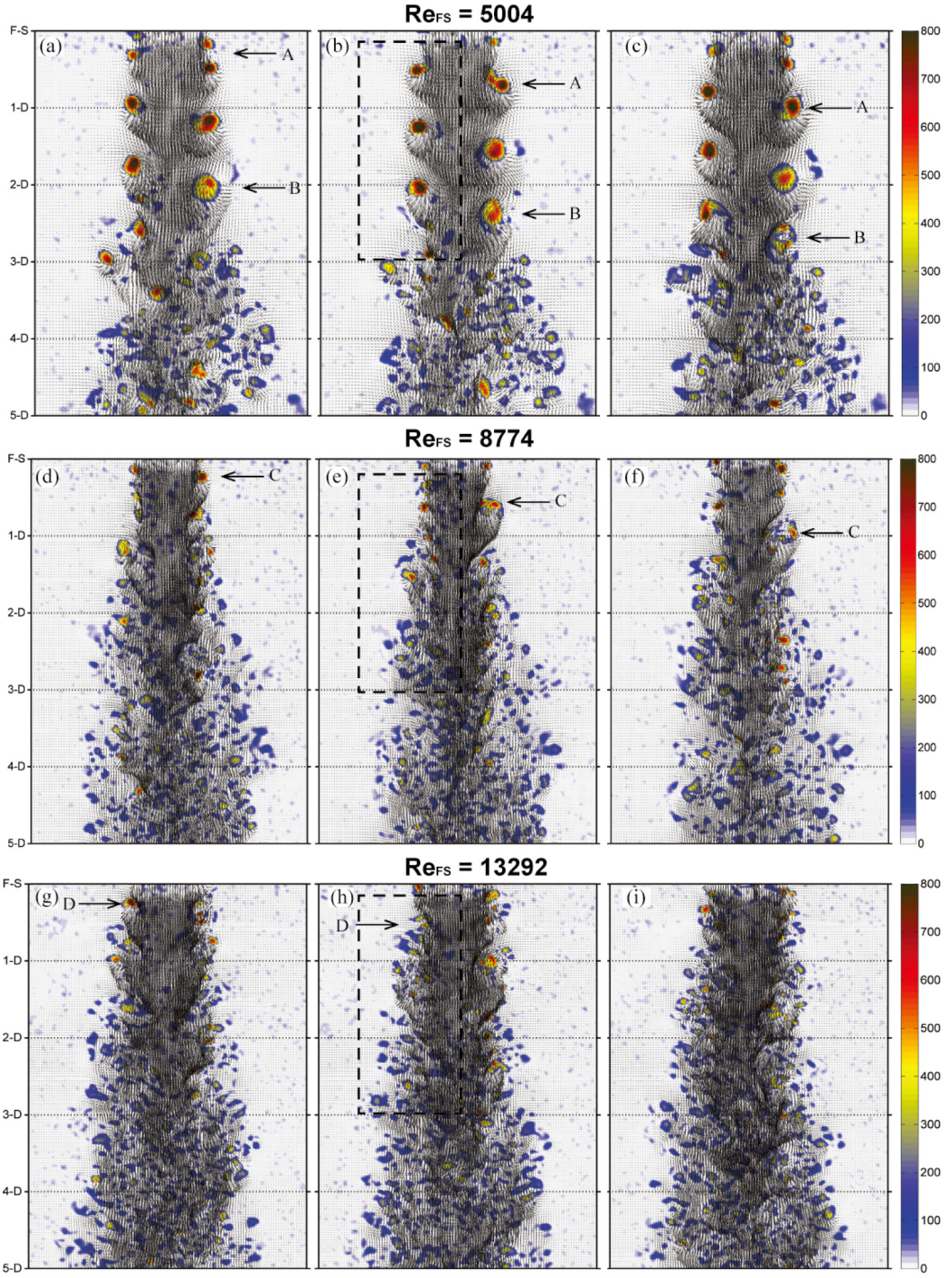

FIG. 8. Time sequence visualization of the plunging jet at $Re_{FS} = 5004$, 8774, and 13 292. Isocontours represent swirling strength of coherent structures (λ_{ci}). Time separation between snapshots: $3\Delta t = 6.12$ ms. The dashed windows (black) show spatial locations plotted in Fig. 9.

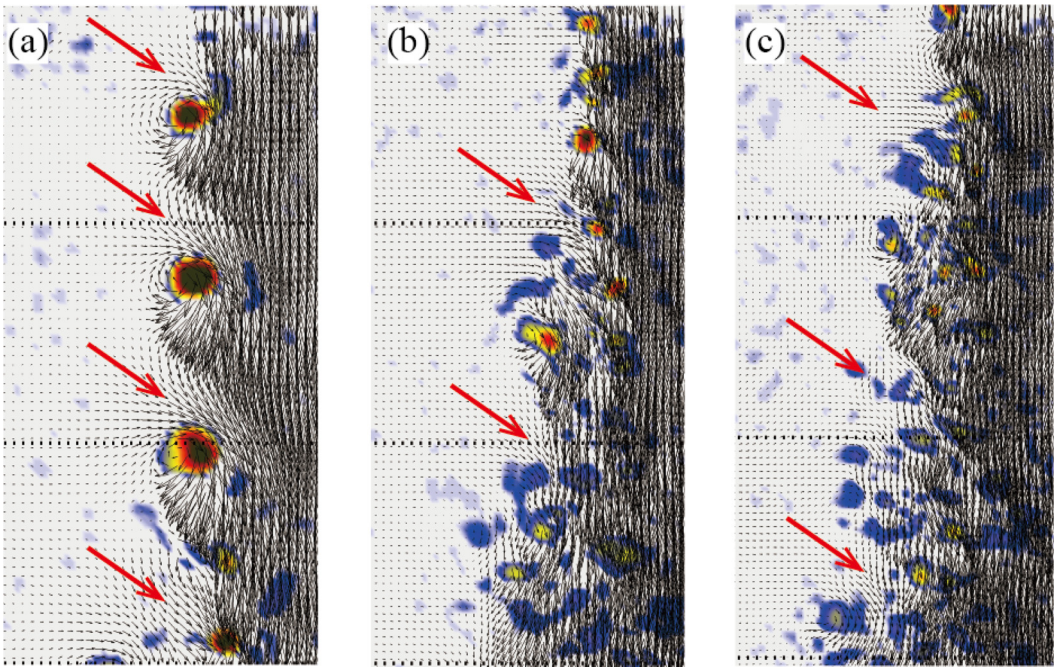

FIG. 9. Close-up view of the initial shear layer of plunging jets at (a) $\mathrm{Re_{FS}} = 5004$, (b) $\mathrm{Re_{FS}} = 8774$, and (c) $\mathrm{Re_{FS}} = 13\,292$ taken from Fig. 8 (black dashed windows). Red arrows show entrainment zones besides primary and secondary vortices.

with lower swirling strength result in weak and disorganized entrainment zones [red arrows in Figs. 9(b) and 9(c)]. In comparison with the previous case at $\mathrm{Re_{FS}} = 5004$, both pairing and disintegration events have shifted upstream to $y/D_{\mathrm{FS}} = 0.3$–0.5 and $y/D_{\mathrm{FS}} = 0.5$–1, respectively [arrows C and D in Figs. 8(d)–8(h)].

IV. DISCUSSION

In this study, statistical flow properties of plunging jets such as mean centerline velocity decay, rms velocity fluctuations, and unsteady flow behavior involving vortex dynamics are analyzed from SPIV measurements. Moreover, we have provided a comparison study on mean entrainment of an ambient fluid between plunging and free jets.

A. Comparison between plunging jet and free jet

When compared with free submerged jets of similar Reynolds numbers, the increased turbulent intensities in the shear layer [42] and faster decay of centerline velocity [43] of plunging jets are usually attributed to the liquid-bubble interaction. This is supported by the comparisons of the flow field between free jet and plunging jet with entrained air bubbles which are widely available in the literature. As for plunging jets without entrained air bubbles, Qu *et al.* [30] recently measured flow fields of submerged and plunging jets with and without air entrainment using PIV, and reported increased velocity fluctuations and faster centerline velocity decay in the absence of entrained air bubbles (Fig. 14 in the cited paper) for plunging jets at $\mathrm{Re} = 5325$. As a result, a shorter potential core was evident when compared with the submerged free jet cases, and the fluid particles were believed to be entrained into the jet region directly at the free surface which results in an earlier start of the fluid entrainment region. They attributed this to the increased impacting jet velocity at the free surface due to gravitational acceleration and induced surface instabilities, given there is no liquid-bubble interaction in the jet region below the free surface.

As a matter of fact, in addition to the aforementioned liquid-bubble interaction and increased impacting jet velocity, there is yet another mechanism responsible for the increased velocity fluctuations and faster centerline velocity decay. This can only be revealed by investigating the instantaneous flow structures in the near field of plunging jets without air entrainment. In the current study, this additional mechanism is well presented by visualization of the formation and evolution of primary vortices that appear immediately below the free surface for all plunging jet cases with no air entrainment. On the contrary, it is well known that for free jets in the same Reynolds number range, it takes approximately 2–2.5 nozzle diameters for the Kelvin-Helmholtz instabilities to develop and accumulate in the shear layer, and finally lead to vortex formation as shown in previous studies [8–10,38]. Although the mechanism for shear layer roll-up is the same, i.e., velocity difference between the high-speed jet column and the ambient quiescent fluid [2,8], for plunging jets, surface disturbance accelerates this roll-up by feeding additional instability. Due to the nature of weakly viscous flow systems, the surface instability was hypothesized by previous researchers [42,44] to be responsible for air entrapment and further flow evolution at higher plunging jet velocity when air bubbles are present. In this study, by intentionally limiting the pump flow rate, this instability was not strong enough to cause air pocket entrapment, but still resulted in early vortex development.

As the primary vortices travel downstream, they accumulate more vorticity in the shear layer, grow in size and strength, undergo mutual induction, and later break up into secondary structures. The evolution of the primary vortices as shown in Figs. 8 and 9 exhibits behaviors very similar to the primary vortices developed in free jets which appear further downstream. The vortex dynamics recapitulate in the following three aspects. First, they facilitate bulk entrainment of the ambient fluid by vortex induction, which results in an early initiation of the entrainment zone and higher near-field entrainment coefficients. At $\mathrm{Re_{FS}} = 5004$, the entrainment coefficient C_E of 0.7 at $y/D_{\mathrm{FS}} = 8$ is more than twice the value reported by Ricou and Spalding for free jets at $\mathrm{Re} > 25\,000$. At the same axial distance, a plunging jet at $\mathrm{Re_{FS}} = 6086$ has $C_E = 0.5$, while entrainment coefficients for the latter three cases collapse along the axial length and reach a value of 0.4. Second, early development of the vortex structures shifts the peaks of rms velocity fluctuations along the centerline further upstream. While previous studies on free jets show that peak fluctuations occur at $y/D = 8$–9 [7,13], the plunging jets in the current study show that peak values for rms velocity fluctuations occur at $y/D_{\mathrm{FS}} = 4$–5 [Fig. 6(a)]. Finally, the early entrainment and velocity fluctuations lead to enhanced momentum diffusion from the jet core toward the ambient liquid and cause premature erosion of the potential core. Subsequently, decay of the centerline velocity starts at $y/D_{\mathrm{FS}} = 2$–2.5 for plunging jets in the range $\mathrm{Re_{FS}} = 5004$–$13\,292$ (Fig. 5), while previous studies show that for free jets, this decay usually starts at $y/D_{\mathrm{FS}} = 5$–7 over a wide range of Reynolds numbers between 5000 and 130 000.

In summary, additional instabilities accumulated from the free surface facilitate vortex development in the shear layer, leading to early initiation of bulk fluid entrainment, and finally result in expedited closure of the shear layer, which is absent for submerged free jets. Thus, along with liquid-bubble interaction, this serves as an additional mechanism responsible for the increased rms velocity fluctuations and faster decay of the centerline velocity of plunging jets when compared with free jets. This mechanism has been overlooked by most of the researchers partially because the majority of the literature has been focused on empirical relationships between penetration depth, air entrainment rate, and inception velocity with plunging jet configurations. Additionally, earlier experimental works were limited to intrusive pointwise local velocity measurement techniques like hot-film probes, pitot tubes, and laser Doppler velocimetry (LDV) [43,45,46], which were not capable of delivering reliable measurement of global flow field, especially near the free surface.

B. Increased entrainment efficiency for low Re plunging jets

Among the plunging jets, the $\mathrm{Re_{FS}} = 5004$ case has higher levels of rms velocity fluctuations which lead to higher turbulent intensity and enhanced mixing that facilitate mass and momentum transfer from the shear layers toward the jet centerline, resulting in higher entrainment efficiency. This relationship was initially explored by Crow and Champagne [7] in their study on excitation

of free jets. They demonstrated that forcing the jet at various excitation frequencies inflated the turbulent intensities along the centerline in the near field, resulting in increased levels of entrainment (Fig. 29 of the cited paper). Higher levels of entrainment have also been correlated with increased turbulent intensity in a recent study by Quinn *et al.* [47] on circular and triangular jets in which they reported that the latter were able to entrain a greater amount of fluid owing to higher turbulent intensity along the centerline (Figs. 6 and 9 of the cited paper).

Higher levels of rms velocity fluctuations that lead to increased entrainment efficiency are due to the presence of strong primary vortices in the shear layer at $\mathrm{Re}_{\mathrm{FS}} = 5004$, a phenomenon that is significantly weak in the latter cases. As these vortices convect downstream, they entrap a large amount of ambient fluid and eventually disintegrate at $y/D_{\mathrm{FS}} = 2.5$–3 into smaller secondary structures. The location where disintegration occurs (arrows B in Fig. 8) agrees well with the initiation of centerline velocity decay (Fig. 5) for $\mathrm{Re}_{\mathrm{FS}} = 5004$. This agreement was also reported by Liepmann and Gharib [8] for a free jet at $\mathrm{Re} = 5500$. They termed this as the mixing transition and explained that disintegration occurs because the velocity difference between the ambient fluid and the high-speed core decreases, attenuating the shear that supports the vortices. For the latter cases at $\mathrm{Re}_{\mathrm{FS}} = 8774$ and 13 292, the location where vortices disintegrate ($y/D_{\mathrm{FS}} = 0.5$–1) does not coincide with the location of the centerline velocity decay ($y/D_{\mathrm{FS}} \sim 2$). The reason for this discrepancy lies in the mechanisms of vortex decay and destruction. At low Reynolds numbers, vortices generated in the shear layer can grow until the end of the potential core [8,10,11]. On the contrary, at high Reynolds numbers, the development of the shear layer is rapid which results in quick decay of the vortical structures and subsequent generation of fine-scale turbulence that suppresses large-scale mixing. This is in agreement with observations of Kim and Choi [11] in their large eddy simulation study and Todde *et al.* [10] in their experimental study on the structure of low Reynolds number free jets.

Recently, several high-resolution computational and experimental studies on free jets and boundary layers have reported results of rigorous analysis on the characteristics of mass entrainment at the turbulent-nonturbulent interface (TNTI) [48–51]. By means of mass-flux spectra, it has been shown that entrainment is a two-stage process that occurs on two different scales with substantial scale separation. The first stage involves "bulk entrapment" of fluid across the TNTI by large eddies of the same scale as the jet diameter. These eddies also give the TNTI its characteristic shape that consists of indentations on a variety of macroscales. The second stage involves "nibbling" that occurs on the order of the Taylor microscale and is independent of the large-scale motions [48]. Nibbling is carried out by a thin viscous "superlayer" that resides on the large-scale indentations and has high levels of vorticity [48–51]. In this two-stage process, the large eddies are responsible for (a) bulk entrapment of ambient nonturbulent fluid across the interface and (b) providing a larger surface area to the TNTI so that the second-stage nibbling process occurs more efficiently [49]. Applying this analogy to the plunging jet cases, we believe that higher entrainment efficiency at $\mathrm{Re}_{\mathrm{FS}} = 5004$ occurs because of large primary and secondary vortical structures that are responsible for the convoluted shape of the TNTI facilitating both bulk entrapment of the ambient fluid and small-scale nibbling due to larger surface area. At higher Reynolds numbers, primary and secondary vortices saturating the TNTI are smaller with less swirling strength, resulting in small-scale indentations and an overall reduced surface area. This suppresses bulk entrapment of ambient fluid and the small-scale nibbling process that is dependent on the TNTI area, leading to overall reduced entrainment efficiency.

V. CONCLUSION

The flow field evolution and ambient fluid entrainment in a plunging jet is investigated between nozzle Reynolds numbers of 3000 and 10 000 (free surface Reynolds numbers of 5004 and 13 292) with time-resolved stereo particle image velocimetry (SPIV). The plunging effect alters the flow field evolution by changing the unsteady flow structure beneath the free surface. Primary vortical structures are formed right below the free surface resulting in an early initiation of entrainment. Early formation of primary vortices further leads to early vortex pairing and

breakdown, resulting in premature closure of shear layers and cessation of the potential core. This is also evident from the statistical flow properties where the locations of centerline velocity decay and peak activity in rms velocity fluctuations occur approximately 4–5 jet diameters upstream of the same locations for free jets in previous studies.

This study presents an effort to quantify ambient fluid entrainment in plunging jets. Due to early development, plunging jets exhibit higher levels of entrainment in the near field compared to free jets. Entrainment values decrease with an increase in Reynolds number and become independent of the same beyond $\mathrm{Re}_{\mathrm{FS}} = 9000$. Early development and higher levels of entrainment also show that plunging jets are not as efficient as free jets in conserving momentum and therefore have better mixing characteristics.

Although current study is focused on a special case of plunging jets where no air entrainment is present, the experimental setup can also be used to visualize the bubble-jet interaction and measure the two-phase flow dynamics near plunger jets when an entrained air bubble is present. Future work may also include extending the measurement domain in the axial direction and using tomographic PIV to fully resolve the three-dimensional near-field flow structure. This would provide more accurate fluid entrainment results by directly integrating the whole three-dimensional flow field rather than assuming axisymmetry.

[1] A. K. Biń, Gas entrainment by plunging liquid jets, Chem. Eng. Sci. **48**, 3585 (1993).
[2] K. T. Kiger and J. H. Duncan, Air-entrainment mechanisms in plunging jets and breaking waves, Annu. Rev. Fluid Mech. **44**, 563 (2012).
[3] T. Massalha and R. M. Digilov, The shape function of a free-falling laminar jet: Making use of Bernoulli's equation, Am. J. Phys. **81**, 733 (2013).
[4] M. J. Hancock and J. W. M. Bush, Fluid pipes, J. Fluid Mech. **466**, 285 (2002).
[5] H. A. Becker and T. A. Massaro, Vortex evolution in a round jet, J. Fluid Mech. **31**, 435 (1968).
[6] A. J. Yule, Large-scale structure in the mixing layer of a round jet, J. Fluid Mech. **89**, 413 (1978).
[7] S. C. Crow and F. H. Champagne, Orderly structure in jet turbulence, J. Fluid Mech. **48**, 547 (1971).
[8] D. Liepmann and M. Gharib, The role of streamwise vorticity in the near-field entrainment of round jets, J. Fluid Mech. **245**, 643 (1992).
[9] D. Violato and F. Scarano, Three-dimensional evolution of flow structures in transitional circular and chevron jets, Phys. Fluids **23**, 124104 (2011).
[10] V. Todde, P. G. Spazzini, and M. Sandberg, Experimental analysis of low-Reynolds number free jets: Evolution along the jet centerline and Reynolds number effects, Exp. Fluids **47**, 279 (2009).
[11] J. Kim and H. Choi, Large eddy simulation of a circular jet: Effect of inflow conditions on the near field, J. Fluid Mech. **620**, 383 (2009).
[12] C. D. Winant and F. K. Browand, Vortex pairing: The mechanism of turbulent mixing-layer growth at moderate Reynolds number, J. Fluid Mech. **63**, 237 (1974).
[13] K. B. M. Q. Zaman and A. K. M. F. Hussain, Vortex pairing in a circular jet under controlled excitation. Part 1. General jet response, J. Fluid Mech. **101**, 449 (1980).
[14] B. Ganapathisubramani, E. K. Longmire, and I. Marusic, Investigation of three dimensionality in the near field of a round jet using stereo PIV, J. Turbul. **3**, N16 (2015).
[15] M. El Hassan and A. Meslem, Time-resolved stereoscopic particle image velocimetry investigation of the entrainment in the near field of circular daisy-shaped orifice jets, Phys. Fluids **22**, 035107 (2010).
[16] K. R. Sreenivas and A. K. Prasad, Vortex-dynamics model for entrainment in jets and plumes, Phys. Fluids **12**, 2101 (2000).
[17] F. P. Ricou and D. B. Spalding, Measurements of entrainment by axisymmetrical turbulent jets, J. Fluid Mech. **11**, 21 (1961).
[18] B. J. Hill, Measurement of local entrainment rate in the initial region of axisymmetric turbulent air jets, J. Fluid Mech. **51**, 773 (1972).

[19] D. Han and M. G. Mungal, Direct measurement of entrainment in reacting/nonreacting turbulent jets, Combust. Flame **124**, 370 (2001).
[20] Y. Zhu, H. N. Oğuz, and A. Prosperetti, On the mechanism of air entrainment by liquid jets at a free surface, J. Fluid Mech. **404**, 151 (2000).
[21] B. Kersten, C. D. Ohl, and A. Prosperetti, Transient impact of a liquid column on a miscible liquid surface, Phys. Fluids **15**, 821 (2003).
[22] W. K. Soh, B. C. Khoo, and W. Y. D. Yuen, The entrainment of air by water jet impinging on a free surface, Exp. Fluids **39**, 498 (2005).
[23] B. W. Atkinson, G. J. Jameson, A. V. Nguyen, G. M. Evans, and P. M. Machniewski, Bubble breakup and coalescence in a plunging liquid jet bubble column, Can. J. Chem. Eng. **81**, 519 (2003).
[24] G. M. Evans, G. J. Jameson, and B. W. Atkinson, Prediction of the bubble size generated by a plunging liquid jet bubble column, Chem. Eng. Sci. **47**, 3265 (1992).
[25] D. Bonsignore, G. Volpicelli, A. Campanile, L. Santoro, and R. Valentino, Mass transfer in plunging jet absorbers, Chem. Eng. Process. **19**, 85 (1985).
[26] A. K. Biń, Minimum air entrainment velocity of vertical plunging liquid jets, Chem. Eng. Sci. **43**, 379 (1988).
[27] K. Yamagiwa and A. Ohkawa, A technique for measuring gas holdup in a downflow bubble column with gas entrainment by a liquid jet, J. Ferment. Bioeng. **68**, 160 (1989).
[28] A. Mandal, G. Kundu, and D. Mukherjee, Gas holdup and entrainment characteristics in a modified downflow bubble column with Newtonian and non-Newtonian liquid, Chem. Eng. Process. **42**, 777 (2003).
[29] F. Z. Kendil, D. V. Danciu, M. Schmidtke, A. B. Salah, D. Lucas, E. Krepper, and A. Mataoui, Flow field assessment under a plunging liquid jet, Prog. Nucl. Energy **56**, 100 (2012).
[30] X. Qu, A. Goharzadeh, L. Khezzar, and A. Molki, Experimental characterization of air-entrainment in a plunging jet, Exp. Therm. Fluid Sci. **44**, 51 (2013).
[31] A. K. Parsad, Stereoscopic particle image velocimetry, Exp. Fluids **29**, 103 (2000).
[32] B. Wieneke, Stereo-PIV using self-calibration on particle images, Exp. Fluids **39**, 267 (2005).
[33] J. Westerweel and F. Scarano, Universal outlier detection for PIV data, Exp. Fluids **39**, 1096 (2005).
[34] T. Guo, M. J. Rau, P. P. Vlachos, and S. V Garimella, Axisymmetric wall jet development in confined jet impingement, Phys. Fluids **29**, 25102 (2017).
[35] L. P. Xia and K. M. Lam, Velocity and concentration measurements in initial region of submerged round jets in stagnant environment and in coflow, J. Hydro-Environ. Res. **3**, 21 (2009).
[36] F. Gori, I. Petracci, and M. Angelino, Flow evolution of a turbulent submerged two-dimensional rectangular free jet of air. Average particle image velocimetry (PIV) visualizations and measurements, Int. J. Heat Fluid Flow **44**, 764 (2013).
[37] H. Fellouah, C. G. Ball, and A. Pollard, Reynolds number effects within the development region of a turbulent round free jet, Int. J. Heat Mass Transfer **52**, 3943 (2009).
[38] T. B. Gohil, A. K. Saha, and K. Muralidhar, Large eddy simulation of a free circular jet, J. Fluids Eng. **136**, 051205 (2014).
[39] L. Boguslawski and C. O. Popiel, Flow structure of the free round turbulent jet in the initial region, J. Fluid Mech. **90**, 531 (1979).
[40] E. J. List, Turbulent jets and plumes, Annu. Rev. Fluid Mech. **14**, 189 (1982).
[41] J. Zhou, R. J. Adrian, S. Balachandar, and T. M. Kendall, Mechanisms for generating coherent packets of hairpin vortices in channel flow, J. Fluid Mech. **387**, 353 (1999).
[42] K. J. Hammad, Liquid jet impingement on a free liquid surface: PIV study of the turbulent bubbly two-phase flow, in *Proceedings of ASME 2010 3rd Joint US–European Fluids Engineering Summer Meeting: Vol.1, Symposia—Parts A, B, and C, 2010* (ASME, New York, 2011), pp. 2877.
[43] K. Harby, S. Chiva, and J. L. Muñoz-Cobo, An experimental study on bubble entrainment and flow characteristics of vertical plunging water jets, Exp. Therm. Fluid Sci. **57**, 207 (2014).
[44] P. D. Cummings and H. Chanson, Air entrainment in the developing flow region of plunging jets—Part 1: Theoretical development, J. Fluids Eng. **119**, 597(1997).

[45] M. Iguchi, K. Okita, and F. Yamamoto, Mean velocity and turbulence characteristics of water flow in the bubble dispersion region induced by plunging water jet, Int. J. Multiphase Flow **24**, 523 (1998).
[46] H. Chanson, S. Aoki, and A. Hoque, Physical modelling and similitude of air bubble entrainment at vertical circular plunging jets, Chem. Eng. Sci. **59**, 747 (2004).
[47] W. R. Quinn, M. Azad, and D. Groulx, Mean streamwise centerline velocity decay and entrainment in triangular and circular jets, AIAA J. **51**, 70 (2013).
[48] K. Chauhan, J. Philip, C. M. de Silva, N. Hutchins, and I. Marusic, The turbulent/non-turbulent interface and entrainment in a boundary layer, J. Fluid Mech. **742**, 119 (2014).
[49] J. Westerweel, C. Fukushima, J. M. Pedersen, and J. C. R. Hunt, Mechanics of the Turbulent-Nonturbulent Interface of a Jet, Phys. Rev. Lett. **95**, 174501 (2005).
[50] C. B. da Silva, J. C. R. Hunt, I. Eames, and J. Westerweel, Interfacial layers between regions of different turbulence intensity, Annu. Rev. Fluid Mech. **46**, 567 (2014).
[51] C. B. Da Silva and R. J. N. Dos Reis, The role of coherent vortices near the turbulent/non-turbulent interface in a planar jet, Philos. Trans. R. Soc., A **369**, 738 (2011).